THE JOURNAL OF PHYSICAL CHEMISTRY LETTERS
A JOURNAL OF THE AMERICAN CHEMICAL SOCIETY

pubs.acs.org/JPCL Letter

Interface-Enhanced Charge Recombination in the Heterojunction between Perovskite Nanocrystals and BiOI Nanosheets Serves as an S-Scheme Photocatalyst for CO_2 Reduction

Atul H. Bhosale, Sudhakar Narra, Sumit S. Bhosale, and Eric Wei-Guang Diau*

Cite This: J. Phys. Chem. Lett. 2022, 13, 7987−7993 Read Online

ACCESS | Metrics & More | Article Recommendations | Supporting Information

ABSTRACT: We designed an S-heterojunction system with a perovskite nanocrystal, $Cs_{1-x}FA_xPbBr_3$ (CF), coupled with a bismuth oxyiodide (BiOI) nanosheet to form a perovskite heterojunction (PHJ) photocatalyst. On the basis of femtosecond transient absorption measurements, the pristine CF sample has two charge recombination periods, 100 and 900 ps, corresponding to surface and bulk trap-state relaxations, respectively. When CF was in contact with BiOI to form an S-heterojunction, rapid interfacial charge recombination occurred to show two decay components with time coefficients 1 and 35 ps, responsible for the electron−hole recombination in the surface and bulk states, respectively. We observed a new photoinduced absorption band on the blue side of the photobleach band of PHJ that gives relaxation more rapid than that of pristine CF, presumably due to doping of bismuth cations creating defect states to enhance the charge recombination that leads to photocatalytic performance for the PHJ catalyst poorer than for the pristine CF sample.

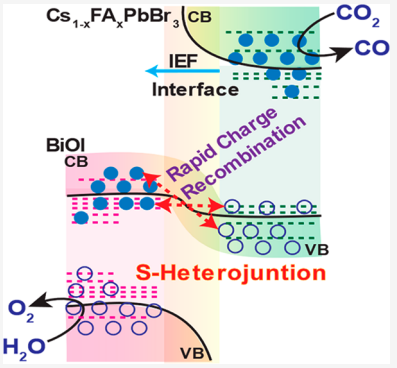

Organic−inorganic halide perovskite nanocrystals (PeNCs) are emerging as efficient photocatalysts for CO_2 reduction[1−4] due to their advantages of facile synthesis, excellent light-harvesting ability, large carrier diffusion length, abundant surface sites, and so on. When PeNC was applied as a photocatalyst for CO_2 reduction with water as a hole scavenger, charge separation occurred upon photoirradiation such that electrons in the conduction band (CB) would be involved in the reduction of CO_2 to generate CO or small carbon species, whereas the holes in the valence band (VB) would be involved in the oxidation of water to generate oxygen. The photocatalytic activities of PeNCs are commonly affected by the charge recombination in the surface and bulk trap states that compete with the redox reactions. To improve their photocatalytic performance, the ability of charge separation should be considered; a hybrid nanostructure composite is a prospective candidate to form perovskite heterojunctions (PHJs) to enhance the charge separation to drive the photocatalytic reactions efficiently.[5−9] Additionally, a heterostructure offers protection on the absorber layers; carrier recombination processes as active sites to drive photocatalytic reactions can be created on the surfaces of ultrathin two-dimensional interfacial layers.[8,10−13] PHJ systems of $MAPbI_3$ with TiO_2,[10] reduced graphene oxide (rGO),[11] and black phosphorus (BP)[12] have been reported; similarly, $CsPbBr_3$ with g-C_3N_4,[13] and MXene[8] sheets were also reported to show excellent conversion yields for H_2 and CO compared with their pristine perovskite films. Zhang et al.[14] reported an S-scheme photocatalyst containing a $CsPbBr_3$ and BiOBr nanocomposite for CO_2 reduction to attain CO production yields better than its pristine catalysts. The formation of S-scheme heterojunction had the effects of enhancing photocatalytic activity and improving the stability of $CsPbBr_3$, but the mechanism of the S-scheme charge transfer is not well understood.

The concept of the S-scheme heterojunction was first reported by Yu and co-workers[15] to replace the conventional terminology of the *Z*-scheme approach.[3,16−18] The spirit of the S-scheme heterojunction is to create an internal electric field from the reduction photocatalyst (RP) toward the oxidation photocatalyst (OP) so that interfacial charge recombination between RP and OP becomes feasible to separate effectively the photoinduced charge carriers for the redox reactions to proceed efficiently. Because several examples have been provided for S-scheme photocatalysts to work properly for CO_2 reduction,[4,14,19,20] it is timely to understand the ultrarapid kinetics of interfacial charge recombination in relation to their photocatalytic performances in a well-defined S-scheme heterojunction system. For this purpose, we designed an S-heterojunction system with a co-cationic cesium formamidinium lead halide perovskite ($Cs_{1-x}FA_xPbBr_3$, abbreviated CF with $x \sim 0.45$) PeNC, a direct-band-gap semiconductor,

Received: July 9, 2022
Accepted: August 18, 2022

https://doi.org/10.1021/acs.jpclett.2c02153
J. Phys. Chem. Lett. 2022, 13, 7987−7993

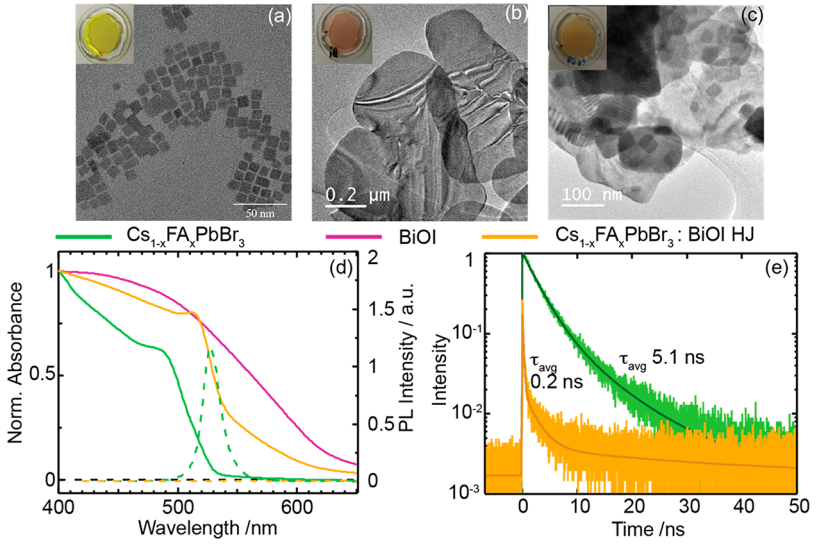

Figure 1. TEM images of (a) CF, (b) BiOI, and (c) PHJ. Photographs of these samples corresponding to use for TAS measurements appear in insets. (d) Absorption (solid curves) and PL (dashed traces) spectra. (e) PL decay profiles obtained from TCSPC measurements for CF and CF:BiOI heterojunction samples as indicated.

coupled with ultrathin bismuth oxyiodide (BiOI) nanosheets, an indirect-band-gap semiconductor.[21] The formation of the S-type heterojunction is confirmed by X-ray photoelectron spectra (XPS). Ultrarapid dynamics of carrier relaxation of pristine CF, BiOI, and hybrid CF/BiOI PHJ samples were investigated with a femtosecond transient-absorption spectral (TAS) technique. We observed interface-enhanced TAS signals with a new photoinduced absorption (PIA) band on the blue side of the photobleach (PB) band of the PHJ sample; the interfacial charge recombination occurs in 1 ps in the surface states and 35 ps in the bulk states. This rapid charge recombination in the S-heterojunction completely quenches the emission of CF. A relaxation mechanism is proposed to interpret the CO production yields appropriately for CO_2 reduction with pristine and PHJ samples as photocatalysts.

$Cs_{1-x}FA_xPbBr_3$ perovskite nanocrystals were synthesized by the method of hot addition;[22,23] ultrathin BiOI nanosheets were synthesized from rubidium bismuth iodide[24] ($Rb_3Bi_2I_9$) PeNC on washing rubidium (Rb) and oxidizing BiI_6 octahedra of Rb PeNC with isopropyl alcohol (IPA) and water.[21] Stirring CF and BiOI powders together for 48 h in toluene produced the CF:BiOI heterojunction samples. Because of the low surface energy of PeNC and strong interaction of the Bi cation with the Br anion of the perovskite, a heterojunction between CF and BiOI was created by simple stirring.[14,19,25,26] The ratio of CF and BiOI in the PHJ sample was adjusted on monitoring the PL intensity of CF PeNC to become completely quenched. Detailed synthetic procedures of the samples are provided in the Supporting Information (SI). The synthesized samples were characterized structurally and morphologically with X-ray diffraction (XRD), energy-dispersive X-ray analysis (EDX), a transmission electron microscope (TEM), and XPS as discussed in what follows.

XRD patterns of the synthesized samples appear in Supporting Information Figure S1. CF PeNC shows broad XRD features indicating that both orthorhombic and cubic phases coexist in these samples;[27] ultrathin BiOI nanosheets display (0,0,k) orientational growth.[28] The XRD patterns of the PHJ sample display signatures of both CF and BiOI signals with minor satellite peaks of the Cs_4PbBr_6 phase.[29] The XRD patterns of the PHJ sample were sharper than those of the CF sample, indicating the increased particle size of the former caused by merging of PeNC via detaching of the ligands from the PeNC. The purity of synthesized BiOI nanosheets and PHJ composition was examined with EDX analysis (Figure S2). BiOI nanosheets displayed excellent purity with Rb atoms in trace proportions; the ratio Bi:I:O was determined to be 1:0.98:1.38 despite a facile approach of washing Rb PeNC with IPA and water, unlike other complicated synthetic routes.[28,30−32] EDX examination of the PHJ film shown in Figure S3 displays a uniform distribution of all elements associated with the formation of PHJ from Cs, Pb, Br, I, and O atoms.

TEM images of the pristine CF sample show uniform cuboids with size over 10 nm; the pristine BiOI sample shows ultrathin nanosheets of size about 400 nm as shown in Figure 1a,b, respectively. Figure 1c shows stacking of CF PeNC on top of ultrathin BiOI nanosheets for the PHJ sample, which confirms the formation of a heterojunction between CF and BiOI. The CF in the PHJ sample shows an increasing size, which is consistent with its sharper XRD signals shown in Figure S1. The increased PeNC size during the formation of PHJ was due to the effect of Ostwald ripening that typically occurred in the liquid samples.[33] The HRTEM image of PHJ in Figure S4 shows that the lattice spacing at the contact is 0.41 nm for PeNC and 0.20 nm for BiOI, both correspond to the (2 0 0) plane. The formation of the (2 0 0) plane for both PeNC and BiOI indicate strong interaction between Br and Bi to form a Bi−Br chemical bond between both species.[14]

The absorption and photoluminescence (PL) spectra of pristine and PHJ samples are shown in Figure 1d. The pristine CF and BiOI samples feature absorption spectral onsets at 525 and 640 nm, respectively. The PHJ sample, in contrast, displays a complicated absorption shape with red-shifted excitonic absorption of CF and a blue-shifted absorption edge of BiOI, an indicator of the formation of a heterojunction. The bathochromic shift of CF absorption spectrum in PHJ might be due to many of the possible reasons such as increased particle size, ion migration at the interface, or offsets of VB/CB bands caused by formation of a heterojunction. It is worth

https://doi.org/10.1021/acs.jpclett.2c02153
J. Phys. Chem. Lett. 2022, 13, 7987−7993

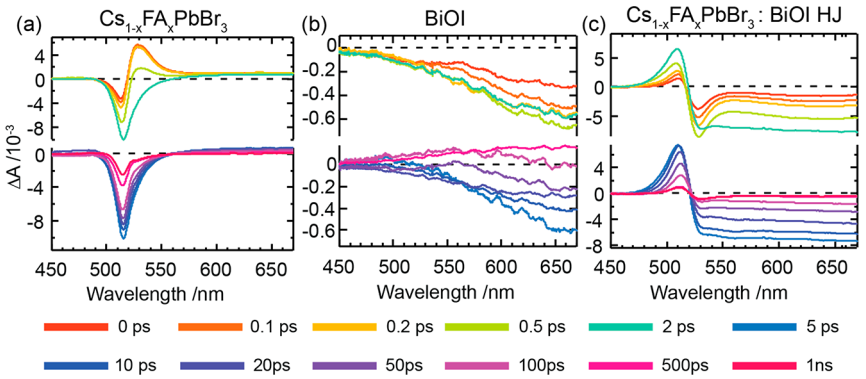

Figure 2. Femtosecond TAS profiles of (a) $Cs_{1-x}FA_xPbBr_3$, (b) BiOI, and (c) $Cs_{1-x}FA_xPbBr_3$:BiOI PHJ samples. The top panels show spectra in intervals 0−2 ps; the bottom panels show spectra in intervals 5−1000 ps. The samples were excited with a femtosecond excitation pulse at wavelength 397 nm, with profiles of temporal evolution in varied intervals as indicated.

noting that the XRD peaks of the CF PeNC in the PHJ sample (Figure S1) did not show any structural changes associated with ion migration, while the EDX results (Figures S2 and S3) showed small fractions of ion exchange and the TEM results (Figure 1a,c) showed substantial increase in particle size. Pristine CF shows bright emission with a maximum at 527 nm; the PHJ sample shows complete quenching of emission due to rapid charge transfer upon irradiation. The PL decays of the pristine CF and PHJ samples were measured using a time-correlated single-photon- counting (TCSPC) technique; the results appear in Figure 1e. The PL decay profile of the CF sample was fitted with a biexponential function whereas that of the PHJ sample with a triexponential function; the corresponding fitted parameters are listed in Table S1. The calculated average PL lifetimes are 5.1 and 0.2 ns for the pristine CF and PHJ sample, respectively. The significantly decreased PL decay lifetime of the PHJ sample is consistent with the quenching of PL intensity shown in Figure 1d due to efficient charge transfer, to be discussed.

The TEM and optical data confirm the formation of a heterojunction between CF and BiOI, but the type of heterojunction[15] is to be discussed. For this purpose, we recorded XPS of the PHJ sample for comparison with those of the pristine samples with the XPS signals of Bi 4f and Pb 4f shown in Figure S5. The pristine BiOI sample shows two lines at 159.8 and 165.1 eV associated with Bi^{3+} $4f_{7/2}$ and $4f_{5/2}$, respectively.[21,28] Similarly, the pristine CF sample displays two lines at 137.8 and 142.7 eV associated with Pb^{2+} $4f_{7/2}$ and $4f_{5/2}$, respectively.[14,19] For the PHJ sample, the XPS signals of Bi 4f shifted to smaller binding energies, whereas those of Pb 4f shifted to greater binding energies, which indicates that electron transfer occurs from CF PeNC to BiOI nanosheets upon formation of the heterojunction through the difference in their work functions.[14,19] Such an electron transfer creates an internal electric field (IEF) pointing from CF to BiOI to align the Fermi levels of the two species and thereby leads to band bending in the interface, so that both CB and VB of CF curve upward whereas those of BiOI curve downward toward the interface. In this way, electrons of BiOI in CB and holes of CF in VB would recombine in the interface between CF and BiOI upon irradiation—a concept for the formation of an S-scheme heterojunction.[15] The formation of the heterojunction was further verified by electron paramagnetic resonance (EPR) spectroscopy; the corresponding results are shown in Figure S6. In dark condition both pristine and PHJ samples do not show any EPR signals. However, under light illumination the PHJ sample shows a progressive increase of EPR signals with stronger intensities than those of pristine CF and BiOI samples, indicating that more photocatalytic sites were activated upon formation of the heterojunction.[34−36] Once the S-scheme heterojunction is formed for the PHJ sample, the electrons in the CB of CF become available for CO_2 reduction to form CO and methane; for the holes in the VB of BiOI water oxidation is feasible to form oxygen, which has been demonstrated for the system of the $CsPbBr_3$ and BiOBr.[14] Because the electron−hole recombination in an S-scheme heterojunction is rapid, the PL of the PHJ sample is significantly quenched; the corresponding PL lifetime decreases within the instrument response limit of TCSPC. A femtosecond spectral technique is hence required to unravel the spectral and kinetic information for the charge recombination in the S-scheme catalyst, with results shown below.

Femtosecond transient-absorption spectra were recorded for pristine and PHJ samples excited with a pulse at 397 nm and probed between 450 and 675 nm; the excitation fluence was 40 $\mu J\ cm^{-2}$. The TAS of pristine CF, BiOI, and PHJ samples appear in Figure 2a−c, respectively. The top panels of Figure 2 show the evolution of the transient bands in delays 0−2 ps; the bottom panels show the recombination of the transient bands in delays 5−1000 ps. The TAS of a pristine CF PeNC sample (Figure 2a) shows a sharp PB band with a maximum at 517 nm and a PIA band on the red side of the spectrum with a maximum at 530 nm. The PIA bands decay rapidly within 1 ps, whereas the PB bands evolve during this period, which is indicative of the thermalization of rapidly generated charge carriers upon excitation. Unlike pristine CF PeNC, the TAS of BiOI nanosheets (Figure 2b) show a weak and broad PB band with depletion maximum centered at 650 nm. The TAS lines of BiOI show a more rapid recovery than those of a pristine CF sample. The TAS signatures of BiOI nanosheets synthesized from Rb PeNC precursors resemble those of earlier reports.[21,37] The TAS of a PHJ sample show both depletion features of a pristine sample with enhanced transient signals, indicating that both species are excited by the femtosecond pulse with an interface-enhanced spectral feature.

Beyond the depletion lines, the PHJ sample also shows an enhanced PIA band on the blue side of the spectrum with a maximum at 510 nm, unlike the transients of a CF sample shown in Figure 2a. The evolution of the blue-side PIA bands in a PHJ sample is much slower than those of the red-side PIA bands in a pristine CF sample. The PIA characteristic on the blue side of the PB band is typically associated with a

https://doi.org/10.1021/acs.jpclett.2c02153
J. Phys. Chem. Lett. 2022, 13, 7987−7993

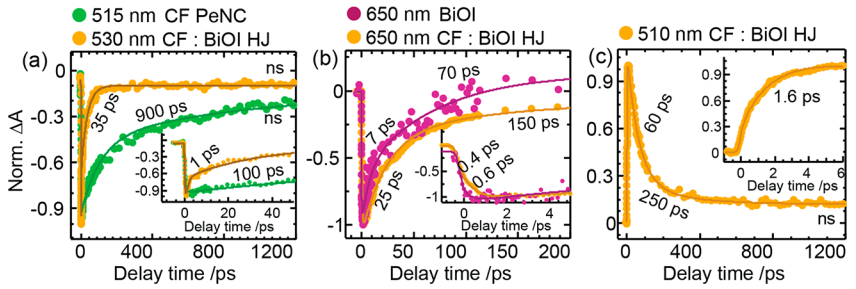

Figure 3. Femtosecond TAS temporal profiles of (a) PB bands of CF (green) and PHJ (orange), (b) PB bands of BiOI (magenta) and PHJ (orange), and (c) PIA band of PHJ (orange) taken at the indicated wavelengths. The fitted time coefficients are indicated.

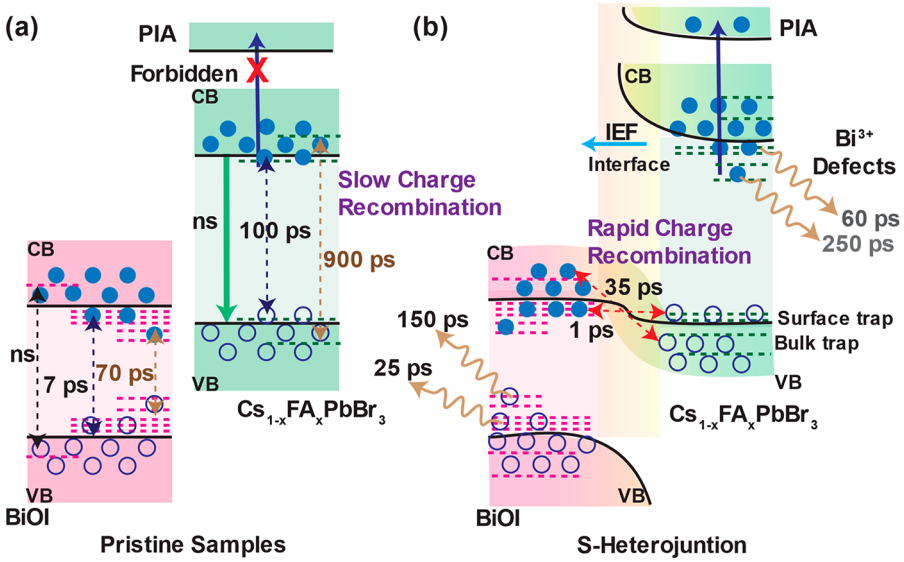

Figure 4. Schematic demonstration showing kinetic models for (a) pristine BiOI and CF and (b) hybrid CF:BiOI heterojunction samples. The blue-side PIA band of CF was symmetry-forbidden but became allowed after Bi doping of the PHJ sample shown in panel b with an interface-enhanced PIA band showing much more rapid electron relaxation than for the slow charge recombination of the pristine CF shown in panel a. IEF represents internal electric field generated in the heterojunction due to the difference of work functions between CF and BiOI.

population of a forbidden excited state or a transient photoinduced phase transition.[37,38] The forbidden excited states become active following photoexcitation through symmetry breaking of the octahedron, which is more pronounced in the presence of defects or doping species.[37,39] This case might apply to the PHJ sample as the ion doping might occur during synthesis of the materials. The origin of the blue-side PIA bands was further clarified on measuring the TAS of a Bi doped CF PeNC sample. The TAS transients of the Bi doped CF sample appear in Figure S7, in which the PIA bands on both blue and red sides of the PB band were observed. The PIA bands on the red side of the PB band were absent in the transients of the PHJ sample because they (corresponding to the hot carriers) were overridden by the interface-enhanced BiOI transient signals shown in Figure 2c. In contrast, the interface-enhanced PIA bands on the blue side of the red-shifted PB band were unambiguously observed in Figure 2c for the PHJ sample because Bi^{3+}-induced surface defects are expected to be involved as the TA spectra of the Bi doped CF sample as shown in Figure S5.

Because the PB band of the PHJ sample was red-shifted by 15 nm from that of the pristine CF sample, we compare the PB recovery kinetics in Figure 3a for a pristine CF sample at 515 nm with a PHJ sample at 530 nm. Figure 3b shows the PB recovery kinetics at 650 nm to compare between pristine BiOI and PHJ samples. Figure 3c shows the PIA band of the PHJ sample at 510 nm corresponding to the interface-enhanced TAS signal that was unobservable for the pristine CF sample. All fitted time coefficients are indicated with the transients shown in Figure 3. For a pristine CF sample, there is a rapid decay (~0.5 ps) on the PIA band at 530 nm and rapid rise on the PB band at 515 nm corresponding to hot-carrier cooling. The recoveries of the PB and PIA bands involve two decay components corresponding to charge recombination through the surface trap (rapid) and bulk trap (slow) states,[40,41] respectively; the ns offset component corresponds to the genuine radiative charge recombination. For a pristine BiOI sample, the rapid rise (~0.5 ps) of the PB band shown in the inset of Figure 3b represents the thermalization of hot carriers, the same as was observed for the CF sample. The rapid and slow recoveries of the PB bands are assigned to shallow and deep trap states, respectively, because the TAS signals were broadly extended to the near-IR region.[21] The PB band recovery of a pristine CF sample at 515 nm shows time coefficients 100 and 900 ps for charge recombination, whereas the PB band recovery of the pristine BiOI sample at 650 nm shows much smaller charge recombination time coefficients, 7 and 70 ps (Figure 4a), because the layered BiOI might involve more surface defects than the CF sample. When CF and BiOI are coupled in the heterojunction sample, the transient of the

https://doi.org/10.1021/acs.jpclett.2c02153
J. Phys. Chem. Lett. 2022, 13, 7987−7993

PB bands of PHJ monitored at 530 nm (to compare with pristine CF at 515 nm) shows significant quenching, with two decay coefficients, 1 and 35 ps (Figure 3a). The PB band of PHJ monitored at 650 nm (to compare with pristine BiOI at 650 nm) shows interface-enhanced signals with decay coefficients 25 and 150 ps (Figure 3b). The quenching of the PB band of CF in the PHJ sample is consistent with the PL quenching observed with the TCSPC decay profiles shown in Figure 1e. The effects of residual zero-dimensional phase Cs_4PbBr_6 (0D) crystals on the charge transfer kinetics between CF and 0D were examined by measuring the TAS of both pristine 0D and the mixed 0D/CF samples, and the corresponding results are shown in Figure S8. The transient profiles shown in Figure S8c indicate that the kinetics of the CF and 0D/CF samples are comparable so that the effect of quenching observed in the PHJ sample due to the existence of a small amount of 0D phase is negligible. Thus, this quenching effect is hence due to the rapid charge recombination between the CF (holes in VB) and BiOI (electrons in CB) as they form an S-type heterojunction with each other for the kinetic model shown in Figure 4b.

After irradiation, the hot carriers relaxed to cold carriers within 1 ps; the electrons in the CB of BiOI then recombined with holes from the surface trap states in 1 ps and those from the bulk trap states in 35 ps when probed at the PB band position of CF. When probed at the PB band position of BiOI, as the electrons at the CB of BiOI recombined with holes at the VB of CF, the holes at the VB of BiOI would have less possibility to recombine with the electrons in the CB; thus hole relaxation alone shows much slower recovery kinetics (25 and 150 ps) than those of the pristine BiOI sample (7 and 70 ps), as we observed in Figure 3b. It is interesting to observe the interface-enhanced PIA band that appeared in the PHJ sample (Figure 2c), for which electrons in the CB of CF were built in 1.6 ps (inset of Figure 3c), probably to reach Bi^{3+}-doped deep surface defect states so that the allowed PIA transition would occur at smaller wavelengths (maximum at 510 nm) with much smaller relaxation time coefficients (60 and 250 ps) than for those of a pristine CF sample (100 and 900 ps). CF and BiOI form a perfect S-scheme heterojunction with much more rapid charge recombination in the interface, but Bi^{3+}-doping of the CF layer in the PHJ sample might create surface defects with rapid charge diminishing to degrade the photocatalytic performance for CO_2 reduction. Our TAS results are consistent with the CO product yields of the photocatalysts generated at the gas−solid interface, showing the trend pristine CF (610 μmol g^{-1}) > PHJ (352 μmol g^{-1}) > Bi:CF (327 μmol g^{-1}) > BiOI (35 μmol g^{-1}), as shown in Figure S9, for which the photocatalytic activity of PHJ is worse than that of a pristine CF catalyst because of the effect of bismuth doping in the PHJ sample that enhances the carrier relaxation in the CB of the CF layer. Another possibility for the observed trend of the performance is the reduction active sites, which are much greater for the CF sample than for the PHJ sample because they were compared on the basis of the same weight of the catalyst. Work is in progress to solve the impurity-doping problem for the S-scheme heterojunction system to retard further the charge recombination on the PeNC so as to enhance its photocatalytic performance.

In conclusion, an S-scheme CF:BiOI photocatalyst was synthesized with a facile low-temperature solution process. The formation of the perovskite heterojunction was characterized with XRD, TEM, XPS, UV−vis/PL, TCSPC, and fs TAS techniques. The XPS data show charge transfer at the interface and confirm the formation of an S-type heterojunction between CF PeNC and BiOI nanosheets. The PL decay profile of the PHJ sample shows average lifetime 0.2 ns, which is significantly smaller than that of a pristine CF sample (5 ns) because of efficient charge recombination at the heterojunction interface. Femtosecond TAS of pristine CF and BiOI samples show predominant spectral and kinetic features associated with relaxations of the carriers from surface and bulk trap states with time coefficients 100 and 900 ps for pristine CF PeNC, respectively; charge recombination occurred at shallow and deep trap states with 7 and 70 ps for a pristine BiOI sample, respectively. For a PHJ sample, formation of an S-heterojunction was confirmed with interface-enhanced PB bands originating from CF and BiOI species, with a newly produced PIA band, not reported elsewhere, at the blue side of the TA spectrum. The new PIA band in the PHJ sample was assigned to an originally forbidden excited-state transition, but it became an allowed transition at shorter wavelengths through doping of Bi^{3+} to break the symmetry and producing deep surface defects. The transient of the PHJ sample probed at the PB band of CF showed a rapid decay with two decay coefficients, 1 and 35 ps, due to charge recombination from surface and bulk trap states, respectively. The PB band of BiOI in the PHJ sample showed retarded decay with time coefficients 25 and 150 ps through a lack of CB electrons for charge recombination. The transient of the new PIA band represents the CB electrons in the CF of PHJ undergoing rapid relaxation due to the Bi^{3+}-doped deep trap defects occurring at the interface, which degraded the photocatalytic activity of CO_2 reduction. The obtained CO product yields at the gas−solid interface showed a systematic order for pristine CF (610 μmol g^{-1}) > PHJ (352 μmol g^{-1}) > pristine BiOI (32 μmol g^{-1}), which is consistent with the corresponding charge relaxation times that exhibit the same trend. The present work reports the first interface-enhanced interfacial relaxation dynamics for the emerging S-scheme photocatalysts and sheds light on the relaxation mechanism for the significance of interfacial defects that might play a key role to improve the photocatalytic performance for S-scheme photocatalysts.

■ ASSOCIATED CONTENT

Supporting Information

The Supporting Information is available free of charge at https://pubs.acs.org/doi/10.1021/acs.jpclett.2c02153.

Experimental methods; (Figures S1−S10) XRD patterns, EDX results, HRTEM image and crystal structure projections, XPS, EPR and TAR spectra, and CO yields; and (Table S1) curve-fitted results (PDF)

■ AUTHOR INFORMATION

Corresponding Author

Eric Wei-Guang Diau − *Department of Applied Chemistry and Institute of Molecular Science and Center for Emergent Functional Matter Science, National Yang Ming Chiao Tung University, Hsinchu 30010, Taiwan;* orcid.org/0000-0001-6113-5679; Email: diau@nycu.edu.tw

Authors

Atul H. Bhosale − *Department of Applied Chemistry and Institute of Molecular Science, National Yang Ming Chiao Tung University, Hsinchu 30010, Taiwan*

https://doi.org/10.1021/acs.jpclett.2c02153
J. Phys. Chem. Lett. 2022, 13, 7987−7993

Sudhakar Narra − *Department of Applied Chemistry and Institute of Molecular Science and Center for Emergent Functional Matter Science, National Yang Ming Chiao Tung University, Hsinchu 30010, Taiwan;* orcid.org/0000-0003-4893-9204

Sumit S. Bhosale − *Department of Applied Chemistry and Institute of Molecular Science, National Yang Ming Chiao Tung University, Hsinchu 30010, Taiwan*

Complete contact information is available at: https://pubs.acs.org/10.1021/acs.jpclett.2c02153

Notes

The authors declare no competing financial interest.

■ ACKNOWLEDGMENTS

We thank Prof. Sue-min Chang and Dr. Aparna K. Kharade for helpful discussions on CO_2 reduction. This work is supported by the National Science and Technology Council (NSTC), Taiwan (Grant Nos. NSTC 111-2634-F-A49-007 and NSTC 111-2123-M-A49-001) and the Center for Emergent Functional Matter Science of National Yang Ming Chiao Tung University (NYCU) from The Featured Areas Research Center Program within the framework of the Higher Education Sprout Project by the Ministry of Education (MOE) in Taiwan.

■ REFERENCES

(1) Wu, L.-Y.; Mu, Y.-F.; Guo, X.-X.; Zhang, W.; Zhang, Z.-M.; Zhang, M.; Lu, T.-B. Encapsulating Perovskite Quantum Dots in Iron-Based Metal-Organic Frameworks for Efficient Photocatalytic CO_2 Reduction. *Angew. Chem.* **2019**, *58* (28), 9491−9495.

(2) Shyamal, S.; Pradhan, N. Halide Perovskite Nanocrystal Photocatalysts for CO_2 Reduction: Successes and Challenges. *J. Phys. Chem. Lett.* **2020**, *11* (16), 6921−6934.

(3) Raza, M. A.; Li, F.; Que, M.; Zhu, L.; Chen, X. Photocatalytic Reduction of CO_2 by Halide Perovskites: Recent Advances and Future Perspectives. *Mater. Adv.* **2021**, *2* (22), 7187−7209.

(4) Bian, H.; Li, D.; Wang, S.; Yan, J.; Liu, S. 2D-C_3N_4 Encapsulated Perovskite Nanocrystals for Efficient Photo-Assisted Thermocatalytic CO_2 Reduction. *Chem. Sci.* **2022**, *13* (5), 1335−1341.

(5) Purohit, S.; Yadav, K. L.; Satapathi, S. Metal Halide Perovskite Heterojunction for Photocatalytic Hydrogen Generation: Progress and Future Opportunities. *Adv. Mater. Interfaces* **2022**, *9*, 2200058.

(6) Akinoglu, E. M.; Hoogeveen, D. A.; Cao, C.; Simonov, A. N.; Jasieniak, J. J. Prospects of Z-Scheme Photocatalytic Systems Based on Metal Halide Perovskites. *ACS Nano* **2021**, *15* (5), 7860−7878.

(7) Kipkorir, A.; DuBose, J.; Cho, J.; Kamat, P. V. $CsPbBr_3$-CdS Heterostructure: Stabilizing Perovskite Nanocrystals for Photocatalysis. *Chem. Sci.* **2021**, *12* (44), 14815−14825.

(8) Pan, A.; Ma, X.; Huang, S.; Wu, Y.; Jia, M.; Shi, Y.; Liu, Y.; Wangyang, P.; He, L.; Liu, Y. $CsPbBr_3$ Perovskite Nanocrystal Grown on MXene Nanosheets for Enhanced Photoelectric Detection and Photocatalytic CO_2 Reduction. *J. Phys. Chem. Lett.* **2019**, *10* (21), 6590−6597.

(9) Zhang, G.; Wang, Z.; Wu, J. Construction of a Z-Scheme Heterojunction for High-Efficiency Visible-Light-Driven Photocatalytic CO_2 Reduction. *Nanoscale* **2021**, *13* (8), 4359−4389.

(10) Wang, X.; Wang, H.; Zhang, H.; Yu, W.; Wang, X.; Zhao, Y.; Zong, X.; Li, C. Dynamic Interaction between Methylammonium Lead Iodide and TiO_2 Nanocrystals Leads to Enhanced Photocatalytic H_2 Evolution from HI Splitting. *ACS Energy Lett.* **2018**, *3* (5), 1159−1164.

(11) Wu, Y.; Wang, P.; Zhu, X.; Zhang, Q.; Wang, Z.; Liu, Y.; Zou, G.; Dai, Y.; Whangbo, M.-H.; Huang, B. Composite of $CH_3NH_3PbI_3$ with Reduced Graphene Oxide as a Highly Efficient and Stable Visible-Light Photocatalyst for Hydrogen Evolution in Aqueous HI Solution. *Adv. Mater.* **2018**, *30* (7), 1704342.

(12) Li, R.; Li, X.; Wu, J.; Lv, X.; Zheng, Y.-Z.; Zhao, Z.; Ding, X.; Tao, X.; Chen, J.-F. Few-Layer Black Phosphorus-on-$MAPbI_3$ for Superb Visible-Light Photocatalytic Hydrogen Evolution from HI Splitting. *Appl. Catal. B Environ.* **2019**, *259*, 118075.

(13) Ou, M.; Tu, W.; Yin, S.; Xing, W.; Wu, S.; Wang, H.; Wan, S.; Zhong, Q.; Xu, R. Amino-Assisted Anchoring of $CsPbBr_3$ Perovskite Quantum Dots on Porous g-C_3N_4 for Enhanced Photocatalytic CO_2 Reduction. *Angew. Chem.* **2018**, *57* (41), 13570−13574.

(14) Zhang, Z.; Li, L.; Jiang, Y.; Xu, J. Step-Scheme Photocatalyst of $CsPbBr_3$ Quantum Dots/BiOBr Nanosheets for Efficient CO_2 Photoreduction. *Inorg. Chem.* **2022**, *61* (7), 3351−3360.

(15) Xu, Q.; Zhang, L.; Cheng, B.; Fan, J.; Yu, J. S-Scheme Heterojunction Photocatalyst. *Chem.* **2020**, *6* (7), 1543−1559.

(16) Kovačič, Ž.; Likozar, B.; Huš, M. Photocatalytic CO_2 Reduction: A Review of Ab Initio Mechanism, Kinetics, and Multiscale Modeling Simulations. *ACS Catal.* **2020**, *10* (24), 14984−15007.

(17) Wu, J.; Huang, Y.; Ye, W.; Li, Y. CO_2 Reduction: From the Electrochemical to Photochemical Approach. *Adv. Sci.* **2017**, *4* (11), 1700194.

(18) Xu, Q.; Zhang, L.; Yu, J.; Wageh, S.; Al-Ghamdi, A. A.; Jaroniec, M. Direct Z-Scheme Photocatalysts: Principles, Synthesis, and Applications. *Mater. Today* **2018**, *21* (10), 1042−1063.

(19) Xu, F.; Meng, K.; Cheng, B.; Wang, S.; Xu, J.; Yu, J. Unique S-Scheme Heterojunctions in Self-Assembled TiO_2/$CsPbBr_3$ Hybrids for CO_2 Photoreduction. *Nat. Commun.* **2020**, *11* (1), 4613.

(20) Fu, J.; Xu, Q.; Low, J.; Jiang, C.; Yu, J. Ultrathin 2D/2D WO_3/g-C_3N_4 Step-Scheme H_2-Production Photocatalyst. *Appl. Catal. B Environ.* **2019**, *243*, 556−565.

(21) Bhosale, A. H.; Narra, S.; Bhosale, S. S.; Liao, P.; Ohta, N.; Diau, E. W.-G. Femtosecond Relaxation Dynamics of Two-dimensional BiOI Nanoplatelets as Efficient Photocatalysts. *J. Chin. Chem. Soc.* **2022**, *69* (1), 51−59.

(22) Bhosale, S. S.; Narra, S.; Jokar, E.; Manikandan, A.; Chueh, Y.-L.; Diau, E. W.-G. Functionalized Hybrid Perovskite Nanocrystals with Organic Ligands Showing a Stable 3D/2D Core/Shell Structure for Display and Laser Applications. *J. Mater. Chem. C* **2021**, *9* (48), 17341−17348.

(23) Bhosale, S. S.; Jokar, E.; Chiang, Y.-T.; Kuan, C.-H.; Khodakarami, K.; Hosseini, Z.; Chen, F.-C.; Diau, E. W.-G. Mn-Doped Organic−Inorganic Perovskite Nanocrystals for a Flexible Luminescent Solar Concentrator. *ACS Appl. Energy Mater.* **2021**, *4* (10), 10565−10573.

(24) Bhosale, S. S.; Kharade, A. K.; Jokar, E.; Fathi, A.; Chang, S.; Diau, E. W.-G. Mechanism of Photocatalytic CO_2 Reduction by Bismuth-Based Perovskite Nanocrystals at the Gas−Solid Interface. *J. Am. Chem. Soc.* **2019**, *141* (51), 20434−20442.

(25) Wang, J.; Wang, J.; Li, N.; Du, X.; Ma, J.; He, C.; Li, Z. Direct Z-Scheme 0D/2D Heterojunction of $CsPbBr_3$ Quantum Dots/Bi_2WO_6 Nanosheets for Efficient Photocatalytic CO 2 Reduction. *ACS Appl. Mater. Interfaces* **2020**, *12* (28), 31477−31485.

(26) Dong, Z.; Zhang, Z.; Jiang, Y.; Chu, Y.; Xu, J. Embedding $CsPbBr_3$ Perovskite Quantum Dots into Mesoporous TiO_2 Beads as an S-Scheme Heterojunction for CO_2 Photoreduction. *Chem. Eng. J.* **2022**, *433*, 133762.

(27) Cottingham, P.; Brutchey, R. L. On the Crystal Structure of Colloidally Prepared $CsPbBr_3$ Quantum Dots. *Chem. Commun.* **2016**, *52* (30), 5246−5249.

(28) Wang, Z.; Chu, Z.; Dong, C.; Wang, Z.; Yao, S.; Gao, H.; Liu, Z.; Liu, Y.; Yang, B.; Zhang, H. Ultrathin BiOX (X = Cl, Br, I) Nanosheets with Exposed {001} Facets for Photocatalysis. *ACS Appl. Nano Mater.* **2020**, *3* (2), 1981−1991.

(29) He, M.; Wang, C.; Li, J.; Wu, J.; Zhang, S.; Kuo, H.-C.; Shao, L.; Zhao, S.; Zhang, J.; Kang, F.; Wei, G. $CsPbBr_3$−Cs_4PbBr_6 Composite Nanocrystals for Highly Efficient Pure Green Light Emission. *Nanoscale* **2019**, *11* (47), 22899−22906.

(30) Di, J.; Xia, J.; Ji, M.; Wang, B.; Yin, S.; Xu, H.; Chen, Z.; Li, H. Carbon Quantum Dots Induced Ultrasmall BiOI Nanosheets with

Assembled Hollow Structures for Broad Spectrum Photocatalytic Activity and Mechanism Insight. *Langmuir* **2016**, *32* (8), 2075−2084.
(31) Prasad, M. D.; Krishna, M. G.; Batabyal, S. K. Facet-Engineered Surfaces of Two-Dimensional Layered BiOI and Au−BiOI Substrates for Tuning the Surface-Enhanced Raman Scattering and Visible Light Photodetector Response. *ACS Appl. Nano Mater.* **2019**, *2* (6), 3906−3915.
(32) Zhang, X.; Ai, Z.; Jia, F.; Zhang, L. Generalized One-Pot Synthesis, Characterization, and Photocatalytic Activity of Hierarchical BiOX (X = Cl, Br, I) Nanoplate Microspheres. *J. Phys. Chem. C* **2008**, *112* (3), 747−753.
(33) DuBose, J. T.; Christy, A.; Chakkamalayath, J.; Kamat, P. V. Transformation of Perovskite Nanoplatelets to Large Nanostructures Driven by Solvent Polarity. *ACS Mater. Lett.* **2022**, *4* (1), 93−101.
(34) Huang, Q.; Ye, J.; Si, H.; Yang, B.; Tao, T.; Zhao, Y.; Chen, M.; Yang, H. Differences of Characteristics and Performance with Bi^{3+} and Bi_2O_3 Doping Over TiO_2 for Photocatalytic Oxidation Under Visible Light. *Catal. Lett.* **2020**, *150* (4), 1098−1110.
(35) Rao, F.; Zhu, G.; Hojamberdiev, M.; Zhang, W.; Li, S.; Gao, J.; Zhang, F.; Huang, Y.; Huang, Y. Uniform Zn^{2+} -Doped BiOI Microspheres Assembled by Ultrathin Nanosheets with Tunable Oxygen Vacancies for Super-Stable Removal of NO. *J. Phys. Chem. C* **2019**, *123* (26), 16268−16280.
(36) Huq, T. N.; Lee, L. C.; Eyre, L.; Li, W.; Jagt, R. A.; Kim, C.; Fearn, S.; Pecunia, V.; Deschler, F.; MacManus-Driscoll, J. L.; Hoye, R. L. Z. Electronic Structure and Optoelectronic Properties of Bismuth Oxyiodide Robust against Percent-Level Iodine-, Oxygen-, and Bismuth-Related Surface Defects. *Adv. Funct. Mater.* **2020**, *30* (13), 1909983.
(37) Rossi, D.; Wang, H.; Dong, Y.; Qiao, T.; Qian, X.; Son, D. H. Light-Induced Activation of Forbidden Exciton Transition in Strongly Confined Perovskite Quantum Dots. *ACS Nano* **2018**, *12* (12), 12436−12443.
(38) Kirschner, M. S.; Diroll, B. T.; Guo, P.; Harvey, S. M.; Helweh, W.; Flanders, N. C.; Brumberg, A.; Watkins, N. E.; Leonard, A. A.; Evans, A. M.; Wasielewski, M. R.; Dichtel, W. R.; Zhang, X.; Chen, L. X.; Schaller, R. D. Photoinduced, Reversible Phase Transitions in All-Inorganic Perovskite Nanocrystals. *Nat. Commun.* **2019**, *10* (1), 504.
(39) Hu, Y. Z.; Koch, S. W.; Lindberg, M.; Peyghambarian, N.; Pollock, E. L.; Abraham, F. F. Biexcitons in Semiconductor Quantum Dots. *Phys. Rev. Lett.* **1990**, *64* (15), 1805−1807.
(40) Narra, S.; Jokar, E.; Pearce, O.; Lin, C.-Y.; Fathi, A.; Diau, E. W.-G. Femtosecond Transient Absorption Spectra and Dynamics of Carrier Relaxation of Tin Perovskites in the Absence and Presence of Additives. *J. Phys. Chem. Lett.* **2020**, *11* (14), 5699−5704.
(41) Socie, E.; Vale, B. R. C.; Burgos-Caminal, A.; Moser, J. Direct Observation of Shallow Trap States in Thermal Equilibrium with Band-Edge Excitons in Strongly Confined $CsPbBr_3$ Perovskite Nanoplatelets. *Adv. Opt. Mater.* **2021**, *9* (1), 2001308.

https://doi.org/10.1021/acs.jpclett.2c02153
J. Phys. Chem. Lett. 2022, 13, 7987−7993